Luminescent rare-earth-doped up-converting nanoparticles for Cr^{3+} sensing in water

Gabriel López-Peña [a], Alejandro Rodríguez García [b], José García Solé [c,d], Emma Martín Rodríguez [a,d,*]

[a] *Departamento de Física Aplicada and Instituto de Ciencia de Materiales Nicolás Cabrera, Universidad Autónoma de Madrid, C/ Francisco Tomás y Valiente 7, 28049, Madrid, Spain*
[b] *Neural Circuits Laboratory, Biosciences Institute, Faculty of Medical Sciences, Newcastle University, NE2 4HH, United Kingdom*
[c] *Departamento de Física de Materiales, Universidad Autónoma de Madrid, C/ Francisco Tomás y Valiente 7, 28049, Madrid, Spain*
[d] *Nanomaterials for BioImaging Group, Instituto Ramón y Cajal de Investigación Sanitaria IRYCIS, Ctra. de Colmenar km 9, 300, 28034, Madrid, Spain*

ABSTRACT

Water contamination by heavy metals poses a significant threat to human health and to the environment. Cr^{3+} is a common contaminant in aqueous media; therefore, innovative sensing technologies for reliable detection are in demand. In this study, we demonstrate that $NaGdF_4$: Yb^{3+}, Er^{3+} up-converting nanoparticles can be used as ratiometric luminescence probes to detect low concentrations of Cr^{3+} contaminating ions in water. Excitation in the near-infrared region provides a fluorescence-based detection method with large depth penetration and is autofluorescence-free. Based on this ability, a paper-based sensor was manufactured in which the incorporated up-converting nanoparticles allowed a limit of detection of Cr^{3+} ion concentrations as low as 2 nM. This represents a new step towards the practical application of rare-earth-doped nanoparticles in environmental monitoring, addressing the critical need for efficient detection methods of contaminating ions in water.

1. Introduction

Owing to great advances in industrial, pharmaceutical, and agricultural fields, environmental contamination has increased, generating different toxic residues, such as heavy metals, pesticides, organic pollutants, and microorganisms [1]. The implications of these contaminants extend beyond human life, affecting animals and plants as well as water, air, and soil. Among the array of contaminants, heavy metals, with their low biodegradability and propensity to accumulate in ecological systems, pose a substantial risk to human and animal health, leading to environmental pollution and contamination of the food chain [2]. Trivalent chromium (Cr^{3+}) ions are of particular concern, as they can be found in small concentrations as contaminants in aqueous media and therefore have a great impact on human health [3]. The maximum safe limits of Cr^{3+} in drinking water were set to 100 μg/L (2 μM) by the United States Environmental Protection Agency (USEPA) and 50 μg/L (1 μM) by the World Health Organization (WHO) [4,5]. Various conventional methods have been developed to detect small concentrations of Cr^{3+} ions in water [6–13]. Optical methods are particularly important

owing to their simplicity and low cost. In this respect, gold nanoparticles (bare or functionalised) have already been used as colorimetric probes to detect Cr^{3+} ion concentrations down to the nanomolar level in different aqueous media [14–16].

Colorimetric methods are based on changes in the absorption spectra of probes (surface plasmon resonance spectrum in the case of gold nanoparticles) as the Cr^{3+} ion concentration is increased. However, they are much less sensitive than luminescence methods, which can detect optical ion concentrations equivalent to optical densities as low as 10^{-8} [17]. Consequently, luminescence-based methods are in high demand because of their high sensitivity, simplicity, and low cost. Yanmei et al. developed a fluorescent chemosensor based on rhodamine that provides a limit of detection (LoD) of 0.023 μM for Cr^{3+} in water [18]. Chengfeng et al. used carbon quantum dots as fluorescence probes to detect low Cr^{3+} ion concentrations in H_2O_2 aqueous solutions [19]. These luminescence methods are based on excitation with ultraviolet or visible light, thus providing low penetration and possible interference with autofluorescence.

Up-converting nanoparticles (UCNPs) are characterised by

---

converting near-infrared (NIR) excitation light into visible-light luminescence. Among the different UCNPs, rare earth co-doped nanocrystals are characterised by a high conversion efficiency of near-infrared (NIR) light into visible or ultraviolet luminescence via suitable multiphoton excitation mechanisms. UCNPs can also be easily dispersed in aqueous media using suitable coatings and properly functionalised for specific targeting purposes. These properties have allowed many applications in analytical and biomedical sciences [20]. The possibility of NIR excitation allows for high depth penetration in water and tissues and strongly reduces autofluorescence, providing highly sensitive biological and chemical sensing [21]. Consequently, UCNPs are particularly suitable for the detection of ionic contaminants in aqueous media. Baoxia et al. used Lysine acid-capped NaYF$_4$: Yb/Er UCNPs together with acid-capped gold nanoparticles for the detection of low Cr^{3+} concentrations in urine [22]. This method was based on the variation in the nonradiative energy transfer efficiency from the UCNPs to the gold nanoparticles as the Cr^{3+} ion concentration increased. More recently, Shijiang et al. used core (LiYF$_4$/Yb^{3+}/Ho^{3+}/Ce^{3+})-shell (LiYF$_4$) UCNPs, whose surface was modified with a Cr^{3+}-sensitive rhodamine derivative to target low Cr^{3+} concentrations via nonradiative Er^{3+} → Cr^{3+} energy transfer [23].

In this study, bare (non-functionalised) NaGdF$_4$:20 % Yb^{3+}, 2 % Er^{3+} UCNPs (Yb, Er-NPs) were used to detect low Cr^{3+} concentrations in water. The method is based on the different reabsorptions of the main green and red Er^{3+} ion luminescence bands due to the Cr^{3+} ions. In particular, the red/green emission intensity ratio linearly increases with Cr^{3+} ion concentration, thus providing a ratiometric and simple luminescence method.

Paper-based sensors have emerged as a superior choice for environmental monitoring, offering a cost-effective porous substrate with straightforward fabrication processes coupled with the inherent portability of paper. Moreover, factors such as biocompatibility, porosity, and easy functionality of this material make paper one of the best choices for sensing applications [24–26]. The remarkable properties of paper-based sensors have paved the way for their successful application in the detection of various contaminants such as heavy metals [27–30], pesticides [31–34], and halides [35,36]. These sensors take advantage of the beneficial properties of paper and provide an accessible, inexpensive, and user-friendly platform for contamination analysis.

Thus, based on the ability of Yb, Er-NPs to detect traces of Cr^{3+} ions in water, a paper-based sensor was manufactured by integrating these nanoparticles into paper substrates. The successful integration of Yb and Er-NPs in paper substrates has enabled a precise, rapid, and substrate-free autofluorescence method for detecting Cr^{3+} ions with an LoD of 2 nM. In fact, the sensitivity of the Yb, Er-NPs in the paper-based sensor clearly increased with respect to that in aqueous solutions. This increase in sensitivity has been properly explained as due to the modification of the Cr^{3+} absorption bands in the paper substrate in respect to those measured in the water solution.

2. Materials and methods

2.1. Materials. Synthesis and characterisation

NaGdF$_4$:20 % Yb^{3+} and 2 % Er^{3+} nanoparticles were synthesised using a standard thermal decomposition method. A mixture containing 2.5 mmol of GdCl$_3$, ErCl$_3$, and YbCl$_3$, 25 mL of octadecene, and 25 mL of oleic acid was heated to 120 °C under vacuum for 1 h, followed by the addition of 0.85 g of sodium trifluoroacetate. Subsequently, the temperature was increased to 300 °C for 2 h under argon atmosphere.

Because the oleate layer of Yb, Er-NPs prevents them from dispersibility in water owing to its hydrophobic nature, the oleate layer was removed following a standard protonation process in acidic media [37]. The oleate-coated nanoparticles were dispersed in hexane (1 mL of hexane for every 10 mg of nanoparticles), and once a stable dispersion was obtained, a drop of hydrochloric acid (Atom Scientific, 36 %) was

added to the dispersion to lower the pH of the dispersion to a value close to 4, in order to ensure a pH value lower than the *pK$_a$* value of oleic acid (which is close to 4.8) [38]. This step ensures the protonation of oleic acid on the Yb, Er-NPs' surface and allows them to be dispersed in water, which is an essential requirement for the analysis of polluted waters.

The morphologies and structures of the synthesised Yb, Er-NPs were characterised using various techniques. Statistical analysis of the transmission electron microscopy (TEM) images (Fig. S1A of the Supplementary Material) showed an average size of 33 ± 9 nm (Fig. S1B in the Supplementary Material). Dynamic light scattering (DLS) measurements of the NPs were performed to determine the hydrodynamic size of the NPs and then compare these results with those obtained from TEM analysis. A hydrodynamic diameter of 126 ± 11 nm was obtained for oleate-covered Yb, Er-NPs. In contrast, a hydrodynamic diameter of 44 ± 4 nm was obtained for the ligand-free NPs, showing a clear reduction in size associated with the removal of the oleate layer on the surface of the NPs (Fig. S1C of the Supplementary Material). The polydispersity indexes (PdI) obtained from these measurements were PdI = 1.2 for the oleate-covered NPs and PdI = 0.3 for the ligand-free NPs, denoting that the ligand-free NPs present a monodisperse character when dispersed in water since values higher than 0.7 indicate a polydisperse distribution of the NPs [39]. X-ray diffraction (XRD) analysis was performed on the synthesised NPs to determine whether they presented a pure hexagonal phase, as expected from the synthesis conditions. It was observed that most of the peaks matched the hexagonal phase of NaGdF$_4$ (red pattern in Fig. S1D of the Supplementary Material) but mixed with peaks of the cubic phase. This mixture of phases is usually explained when certain parameters of the synthesis process are met, such as changes in the quality of the solvents that can lead to the formation of some nanoparticles with cubic phases, a slow rise in the temperature when the synthesis is set to 300 °C, or even an unstable argon flow during the last step of the synthesis.

2.2. Methods

2.2.1. Transmission electron microscopy

Transmission electron microscopy (TEM) images were obtained using a JEOL JEM1010 microscope at 100 kV. The samples were prepared by dropping sample dispersions (0.1–0.5 mg/mL in hexane) onto a 300-mesh carbon-coated copper grid (3 mL in diameter) followed by evaporation of the solvent.

2.2.2. Dynamic light scattering and ζ-Potential measurements

DLS measurements were performed with a Zetasizer Nano ZS instrument (Malvern Panalytical, Malvern) using a 0.1 mg/mL dispersion of NPs in hexane (oleate-capped NPs) or deionised water (oleate-free NPs) contained in a standard 1 cm quartz cuvette. The system uses a red laser (630 nm wavelength) as the light source, and the angle between the sample and the detector was 173°.

2.2.3. X-ray diffraction analysis

XRD spectra were obtained from a powder sample of NaGdF$_4$:2 % Er^{3+}, 20 % Yb^{3+} nanoparticles using a Bruker D8 Discover diffractometer with θ – 2θ geometry.

2.2.4. Absorption spectra

Absorption spectra were recorded at room temperature using a double-beam PerkinElmer Lambda 1050 spectrometer. A PerkinElmer 150 mm InGaAs integration sphere module was used to record the extinction spectra of the paper substrates.

2.2.5. Up-conversion emission spectra

A homemade system was used to collect the up-conversion emission spectra. This setup consists of a 980 nm Lumics diode laser for excitation and several mirrors and lenses to collect the emitted light and focus it in an iHR320 HORIBA monochromator with a cooled CCD array Synapse

HORIBA detector. All the spectra were measured at room temperature.

2.2.6. Total reflection X-ray fluorescence

The TXRF studies presented in this work were carried out using a TXRF S2 PICOFOX (Bruker) spectrometer operating at 50 kV using Mo K radiation as excitation.

3. Results and discussion

The Yb, Er-NPs used in this study produced visible emissions under NIR excitation (980 nm). Fig. 1A shows a simplified energy-level scheme explaining the main excitation/emission mechanisms of these nanoparticles [40]. The Yb^{3+} ion absorbs the 980 nm NIR light and is promoted to its $^2F_{5/2}$ excited state; thus, energy transfers take place from this state to the $^4I_{11/2}$ state of Er^{3+}. Subsequently, a second excited Yb^{3+} ion transfers its energy to the $Er^{3+}(^4I_{11/2})$ excited ion, thus populating the $^4F_{7/2}$ excited state of Er^{3+}. The main visible emissions (green and red) are produced after successive nonradiative decays from this state to the $^2H_{11/2}$–$^4S_{3/2}$ and $^4F_{9/2}$ states, from which the green and red emissions are produced by transitions to the ground state ($^4I_{11/2}$). This is a two-step $Yb^{3+} \to Er^{3+}$ up-conversion energy transfer. Alternatively, the red-emitting state ($^4F_{9/2}$) can also be populated if the second $Yb^{3+} \to Er^3$ energy-transfer step populates such a state via the $^4I_{13/2} \to {}^4F_{9/2}$ transition, where the $^4I_{13/2}$ energy state has been previously populated by multiphonon nonradiative decay from the $^4I_{11/2}$ state. These two-step energy transfer competitive processes make the ratio between the red and green Er^{3+} emissions dependent on the Yb^{3+} ion concentration. Indeed, this ratio has been shown to increase with the Yb^{3+} ion concentration in hexagonal $NaYF_4$: Yb, Er nanocrystals [40].

Fig. 1B shows the visible emission spectrum of a 10 mg/mL aqueous dispersion of Yb, Er-NPs under NIR laser excitation (980 nm wavelength). As can be observed, the emission is composed of two main bands: a green one (lying between 500 and 580 nm), and a red one (lying between 620 and 720 nm). The green emission has two main components owing to the $^2H_{11/2} \to {}^4I_{15/2}$ (524 nm) and $^4S_{3/2} \to {}^4I_{15/2}$ (542 nm) transitions of Er^{3+} (see Fig. 1). The red band centred at approximately

655 nm is due to the $^4F_{9/2} \to {}^4I_{15/2}$ transition of Er^{3+}. It is important to mention that the red-to-green emission ratio of Yb, Er-NPs depends on a variety of parameters, such as the crystal phase, particle size, rare earth ion concentrations, and excitation intensity [40–44]. However, the red-to-green ratio observed here (approximately 2) is quite similar to that previously reported for the hexagonal phases of $NaGdF_4$ [43] and $NaYF_4$ [40] nanocrystals with similar sizes, rare earth dopant concentrations, and excitation intensities. This suggests that the emission observed here is due to the hexagonal phase component in our NPs. The water environment may also play a role. Nevertheless, it has been reported that in the hexagonal $NaGdF_4$ phase, the upconversion fluorescence is much brighter than that in the cubic phase [44]. Consequently, we can reasonably assume that the emission spectrum shown in Fig. 1B is mostly due to the hexagonal phase of the nanocrystals.

Fig. 1C shows the absorption spectrum of Cr^{3+} obtained from an aqueous solution with a 20 M concentration of chromium (III) potassium sulphate dodecahydrate. It consists of two broad bands with maxima around 410 and 580 nm, related to transitions within the $3d^3$ electronic configuration of Cr^{3+} ions [45–47]. For comparison, the emission spectrum of Yb, Er-NPs is also shown in Fig. 1C. It can be observed how the green emission bands of the Yb, Er-NPs completely overlap with the absorption band of Cr^{3+} at 580 nm. However, this Cr^{3+} absorption band only partially overlaps with the red emission bands of Yb, Er-NPs. The molar extinction cross section at the peak of this Cr^{3+} absorption band was calculated to be $\varepsilon = 0.14$ $M^{-1}cm^{-1}$, similar to those obtained in other hots [48,49]. Importantly, the molar extinction coefficients of Cr^{3+} at the central wavelengths of the green (533 nm) and red (655 nm) Er^{3+} emissions, $\varepsilon_g = 0.10$ $M^{-1}cm^{-1}$ and $\varepsilon_r = 0.05$ $M^{-1}cm^{-1}$, are very different. Consequently, we expect to observe a remarkably different reabsorption for the red and green emission bands of the Yb, Er-NPs as the Cr^{3+} ion concentration increases. In other words, a significant change in the red-to-green emission intensity ratio of Yb, Er-NPs is expected to occur as the Cr^{3+} concentration increases. Moreover, to ensure the specific selectivity of this ratiometric method for Cr^{3+} ions, the absorption spectra of other common water contaminants were measured (Fig. S2 of the Supplementary Material) in the spectral range
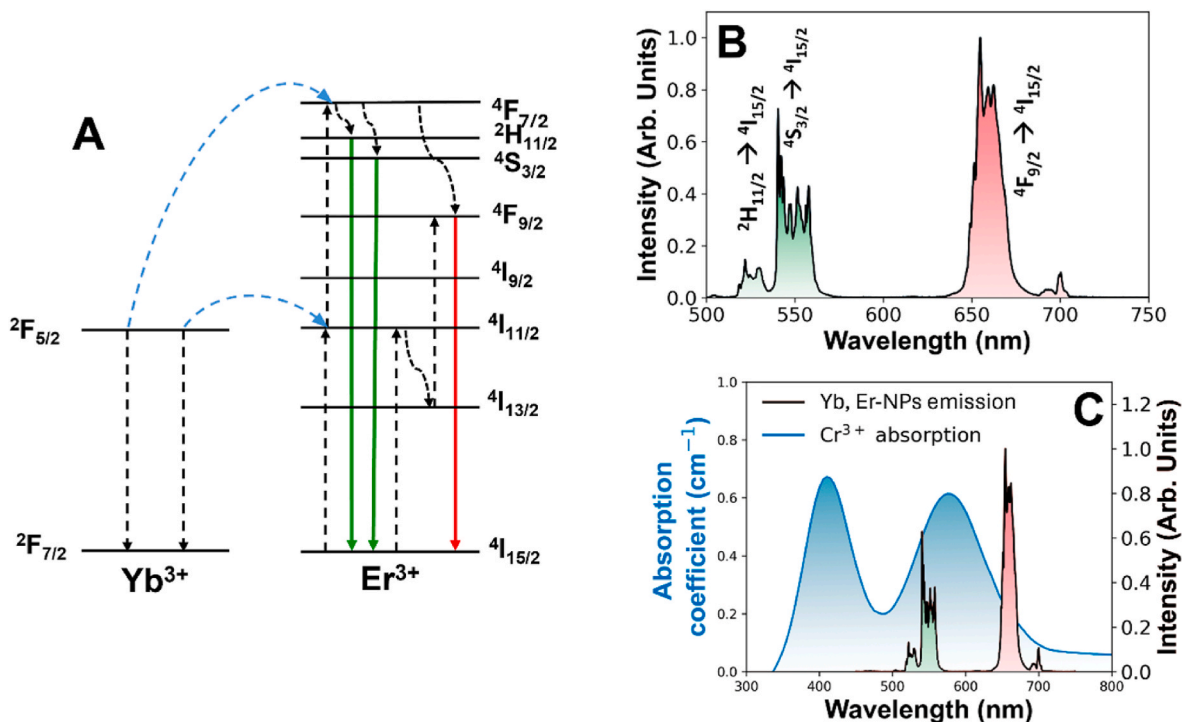

Fig. 1. A. Energy level diagram explaining the up-conversion energy transfer mechanisms of the Yb, Er-NPs used in this study. **B.** Emission spectrum of the NPs. **C.** Absorption coefficient of Cr^{3+} ions and emission spectrum of Yb, Er-NPs.

corresponding to the green and red emissions of Yb, Er-NPs. It was concluded that only Cr^{3+} ions had a significant effect on the emission of Yb, Er-NPs.

The next step of this study was to demonstrate the sensing ability of Yb, Er-NPs for the detection of Cr^{3+} in water. For this purpose, we investigated the changes in the up-conversion emission spectrum of Yb, Er-NPs (Fig. 1B) in the presence of different concentrations of the Cr^{3+} contaminant added to the aqueous solution. To achieve this, different aqueous dispersions of oleate-free Yb, Er-NPs (10 mg/mL) were prepared in combination with different concentrations of Cr^{3+}, ranging between 0 and 1.8 μM. As an example, Fig. 2A shows the visible emission spectrum of a dispersion of Yb, Er-NPs in water (10 mg/mL) in the presence of the different concentrations of Cr^{3+} used in this part of the work. A more detailed figure of the variation in the green emission band with different Cr^{3+} concentrations is shown in Fig. S3 of the Supplementary Material. As expected, the Er^{3+} emission spectrum shows a decrease in the 550 nm green emission band as the Cr^{3+} concentration increased. However, the intensity of the red emission band remains practically unaffected owing to its low reabsorption by Cr^{3+} ions, in agreement with the results previously observed in Fig. 1C. Therefore, the red-to-green emission ratio is a good indicator of the concentration of Cr^{3+} ions in different aqueous solutions. Fig. 2B shows the red-to-green emission ratio (i.e. the total area under the red emission band divided by the total area under the green emission band) as a function of the concentration of Cr^{3+} ions. All experiments were performed using a 980 nm diode laser with a fixed power density of 9.5 mW/cm^2. A linear dependence was clearly observed, thus revealing that, in principle, Yb, Er-NPs provide a fluorescence ratiometric method to determine the content of Cr^{3+}. From these data, the limit of detection (LoD) of the sensor was calculated as $LoD = 3\sigma/m$, where σ is the standard deviation of 10 consecutive measurements of the blank sensor (without Cr^{3+}), and m is the slope of the calibration curve. The LoD indicates the Cr^{3+} lowest concentration that can be detected with certainty. A LoD as low as 5.2 nM was obtained, which indicates the high sensitivity of this method.

In principle, the ability of the Yb, Er-NPs to sense Cr^{3+} should be explained because of the different internal reabsorption of the red and green Er^{3+} ion emission by the Cr^{3+} ions dispersed in the aqueous solution. Nevertheless, to determine the possibility of nonradiative $Er^{3+} \rightarrow Cr^{3+}$ energy transfer, the decay time profiles of the Er^{3+} emissions were measured as a function of the Cr^{3+} content in the aqueous solution. The decay curves showed a rise time (due to the energy transfer from Yb^{3+} to Er^{3+} ions) followed by an exponential decay (Fig. S4 of the Supplementary Material). Fig. 2C shows the evolution of green and red emission lifetimes with increasing concentrations of Cr^{3+} ions. Both the red (196 ± 2 μs) and green (90.0 ± 0.7 μs) emission lifetimes remain constant in the Cr^{3+} concentration range used in this work. This result confirms the absence of emission quenching due to possible nonradiative $Er^{3+} \rightarrow Cr^{3+}$ energy transfer processes. Consequently, the observed results clearly originate from the reabsorption of the green and red Er^{3+} emissions by Cr^{3+} ions dispersed in the aqueous solution.

The linear dependence observed in Fig. 2B can be explained by considering the different molar extinction coefficients of Cr^{3+} at the central wavelengths of the red emission, ε_r (533 nm), and the green emission, ε_g (655 nm), of Er^{3+}, which have been determined above. Thus, according to the Lambert-Beer extinction law, we can write

$$R = \frac{I_{r0} \cdot 10^{-\varepsilon_r Cx}}{I_{g0} \cdot 10^{-\varepsilon_g Cx}} = R_0 \cdot 10^{Cx(\varepsilon_g - \varepsilon_r)} \tag{1}$$

where $R_0 = I_{r0}/I_{g0}$ is the red-to-green intensity ratio at the excitation spot, R is the same ratio measured in the detector, C *is* the molar concentration of Cr^{3+}, and x is the beam path travelled by the emitted light in the aqueous dispersion (i.e. before reaching the detector). For low Cr^{3+} molar concentrations, Equation (1) can be approximated as

$$R \simeq R_0 x \left(\varepsilon_g - \varepsilon_r \right) \cdot C \tag{2}$$

This expression qualitatively explains the linear dependence of the intensity ratio on the Cr^{3+} concentration (Fig. 2B) owing to the different reabsorption of the red and green light emitted by the Yb, Er-NPs by the Cr^{3+} ions dispersed in the aqueous solution. This difference in reabsorption is due to the difference in the molar extinction coefficients ($\varepsilon_g - \varepsilon_r$) of Cr^{3+} at the green and red wavelengths of the Er^{3+} emissions. Indeed, the larger the (ε_g - ε_r) difference, the higher the slope, and thus, the higher the sensitivity.

To ensure that the sensing mechanism is only related to the reabsorption of the Er^{3+} upconversion emissions, the possible pump-induced heating must be discarded. Indeed, this effect could affect the red-to-green emission ratio, since the shape of the green emission band has been shown to be temperature-dependent [50]. This temperature dependence is related to the thermal redistribution in the populations of the $^2H_{11/2}$ and $^4S_{3/2}$ excited states of the Er^{3+} ion. In fact, the ratio of the $^2H_{11/2} \rightarrow {}^4I_{15/2}$ and $^4S_{3/2} \rightarrow {}^4I_{15/2}$ green emissions has previously allowed the use of these nanoparticles as nanothermometers [51]. We can take advantage of this fact to check whether pump-induced heating is produced at the 980 nm excitation intensity used here (9.5 mW/cm^2) by using the above-mentioned green emission intensity ratio as a temperature indicator. Thus, we carefully examined the ratio between the two green emission bands ($R = \text{Area}_{550\,nm}/\text{Area}_{525\,nm}$) as a function of the excitation time. If pump-induced heating occurs (because of water absorption of the 980 nm excitation light), a progressive temperature increase should be expected with the illumination time. As R remained constant even after 10 min of illumination (Fig. S5 of the Supplementary Material), we can ensure that pump-induced heating is negligible under our experimental conditions. Additionally, it is important to note that temperature variation may affect the green emission shape, but not the overall green emission intensity (i.e. the total area under the green emission band). As our method considers the ratio between the areas under the green and red emissions, we consider that in the case of slight changes in temperature during different measurements, this aspect would not be too relevant because we are using the ratio between the
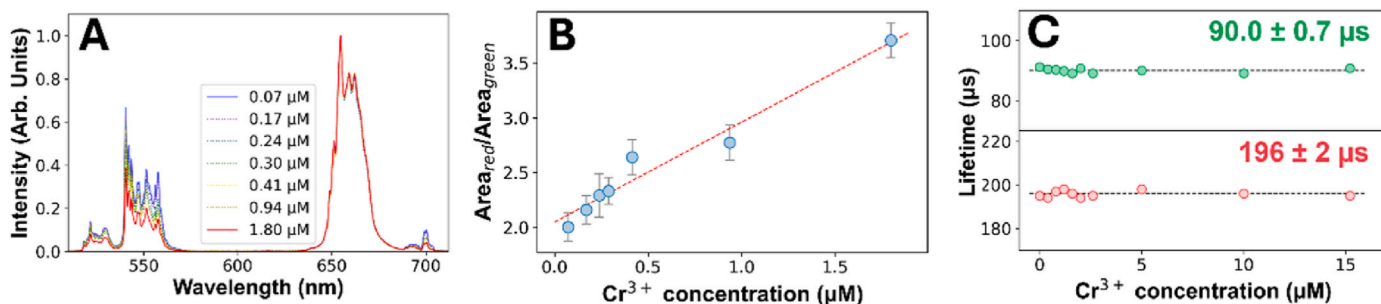

Fig. 2. A. 980 nm excited visible emission spectra of Yb, Er-NPs in the presence of different concentrations of Cr^{3+} ions (excitation intensity 9.5 mW/cm^2). **B.** Calibration curve obtained from the variation in red-to-green emission ratio with Cr^{3+} concentration. The red dotted line was used as a guide for the eye. **C.** Lifetimes of the green (550 nm) and red (650 nm) emission bands as a function of Cr^{3+} concentration. Both black dotted lines are used as eye guides.

areas under the green and red emission bands.

Once the ability of Yb, Er-NPs to sense Cr3 + in water was demonstrated, a paper-based sensor was fabricated using these nanoparticles. According to Equation (2), the slope of the calibration line (red-to-green intensity ratio vs. Cr^{3+} concentration) must change with the light path of the Yb, Er-NP emissions in the water solution. Thus, the sensitivity of the method described in the water solution should be somewhat dependent on the geometrical excitation-emission conditions. In contrast, it is expected that the sensitivity of paper-based sensors is practically independent of the excitation-emission geometrical conditions. To fabricate the paper-based sensor mentioned above, 1.5 × 1.5 cm Whatman chromatography paper (CAT No. 3001-861) was used as the substrate. Yb, Er-NPs were fixed to the paper by immersing them in an Er, Yb-NP dispersion in deionised water (10 mg/mL) for 10 min. The paper sensor was then dried for 20 min at 60 °C following the fabrication method previously reported by Mei et al. [52]. Fig. 3A shows a photograph of the paper-based sensor under 980 nm diode laser illumination, where a green emission in the excited area of the paper-based sensor is clearly observed by the naked eye. This simple result demonstrated the successful incorporation of Yb and Er-NPs into the paper substrate. Fig. 3B shows the up-conversion emission spectrum of Yb, Er-NPs in the paper-based sensor, together with those previously obtained for Yb, Er-NPs in aqueous dispersions (Fig. 1B). Interestingly, the intensity of the green emission band was much higher for the paper-based sensor than for the aqueous solution. This may be due to the different non-radiative mechanisms that are expected to occur for Er^{3+} ions located on the surface of the nanoparticles in both media (water and paper). Indeed, the $^4F_{9/2}$ excited state, responsible for the red emission, is efficiently populated in water because the high-energy OH^- vibrational groups of the water molecules favour the nonradiative decay rate from the $^4S_{3/2}$ state to the $^4F_{9/2}$ emitting state. In fact, the OH^- vibrational groups can act as efficient energy bridges between these two states, substantially reducing the number of emitted phonons to cross the

energy gap between these states, thus increasing the red emission intensity (see Fig. 1A). However, when Yb, Er-NPs are incorporated in the paper, the absence of these high-energy OH^- vibrational groups strongly reduces the above-mentioned nonradiative rate, and thus the red emission intensity decreases while the green emission intensity increases [37]. Consequently, the red-to-green emission ratio must be lower on paper than in an aqueous solution, as observed experimentally (see Fig. 3B). In addition, deactivation of the Yb^{3+}-sensitising ions on the surface of the nanoparticles may also play a role, as it can also affect the Er^{3+} red-to-green emission ratio [53].

The paper-based sensors were submerged during 1 min in various aqueous solutions containing different concentrations of Cr^{3+}, ranging from 0.1 to 3 μM. After drying the paper, the up-conversion emission spectra of the NPs in the paper substrates were measured in four different regions of the paper, and the mean value of these results was used. It is important to mention that the emission spectra were practically independent of both the excited region and excitation-emission geometry. Fig. 3C shows the red-to-green emission ratio (measured with the paper sensor) as a function of Cr^{3+} concentration in water, that is, using different aqueous solutions. The effect of different Cr^{3+} concentrations on the emission spectrum of the Yb, Er-NPs is shown in Fig. S6 of the Supplementary Material. Contrary to what was observed in the Yb, Er-NPs/water experiments, where the trend was linear for all Cr^{3+} concentrations used (see Fig. 2B), it can be observed that the red-to-green emission ratio shows two different tendencies. For Cr^{3+} concentrations lower than 0.5 μM, a linear behaviour was observed (see inset of Fig. 3C), but for higher concentrations, the ratio shows a saturating behaviour, that is, the ratio barely changes with the Cr^{3+} concentration. Importantly, the implementation of Yb, Er-NPs on paper substrates directly affected the sensitivity of the sensor, showing a LoD (calculated from the linear region of the curve) of 2 nM, which is a lower value than that obtained for the Yb, Er-NPs/water experiments (LoD = 5.2 nM).

In principle, the saturation in the red-to-green emission ratio (and so
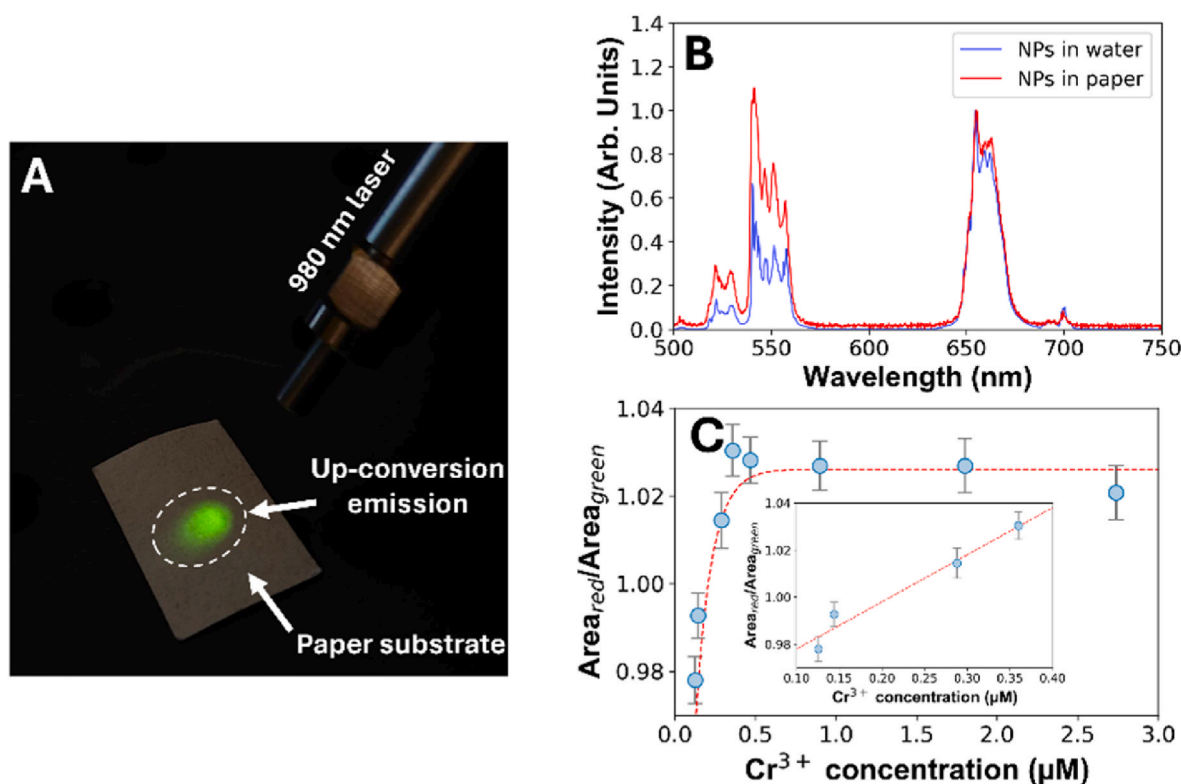

Fig. 3. A. Photograph of the Yb, Er-NPs paper-based sensor under illumination with a 980 nm laser diode. **B.** Emission spectra of Yb, Er-NPs in water and in the paper-based sensor (980 nm laser diode excitation). **C.** Red-to-green emission ratio of the paper-based sensor as a function of Cr^{3+} concentration in water. The red dotted line was used as a guide for the eye.

on the sensitivity) observed for the NPs paper-based sensor could be related to the limit in the amount of chromium that can be incorporated into the paper substrates. Thus, to gain information on the observed saturation behaviour, total-reflection X-ray fluorescence (TXRF) experiments were performed. These experiments allowed the determination of the total amount of chromium incorporated into the paper as a function of the amount of chromium (III) potassium sulphate dodecahydrate (i.e. of Cr^{3+}) in the aqueous solution [54]. Fig. 4A shows a linear behaviour; thus, no saturation behaviour is observed. Thus, the saturation behaviour observed in Fig. 3C must not be due to a limit in the amount of Cr^{3+} incorporated into the paper. In addition, Fig. 4A indicates that only a small percentage (approximately 1 %) of Cr^{3+} was incorporated into the paper.

At this point, we would like to explain the features of our paper-based detector, that is, the saturating behaviour observed in Fig. 3C–as well as the increase in sensitivity with respect to the Yb, Er-NP/water sensor. For this purpose, we now analyse how the visible absorption spectrum in paper substrates evolves with the amount of chromium in these substrates. Because this concentration is proportional to the Cr^{3+} concentration in water, it determines the sensing behaviour of the paper-based sensor. For this purpose, the absorption spectra of different paper-based sensors with different chromium concentrations (ranging from 0.1 to 3 μM) were measured using an integration sphere. The results are shown in Fig. 4B. It can be clearly observed that the paper shows an absorption edge towards the ultraviolet region, adding a component to the Cr^{3+} absorption bands. Indeed, when chromium was added to the paper, the absorption band of Cr^{3+} at 580 nm was still clearly observed in the spectrum. In addition, the absorption edge (300–500 nm spectral region) increased with chromium concentration, masking the other band around 400 nm that appeared for Cr^{3+} ions dispersed in water. The nature of this absorption edge is presently unknown, but it could be tentatively explained by the appearance of a new charge-transfer band involving chromium ions. Nevertheless, regardless of the nature of this edge, the red-to-green emission ratios of Yb and Er-NPs must be modified. Thus, using different absorption spectra, we measured the absorption of red and green light within the spectral ranges corresponding to the red and green emissions of Yb, Er-NPs (610–720 nm and 500–580 nm, respectively) as a function of chromium concentration in the paper substrate. Fig. 4C shows the red-to-green absorption ratio as a function of chromium concentration in the paper substrate. As observed, this ratio decreases with chromium concentration up to approximately 5 nM, but remains unchanged for higher chromium concentrations. This explains the experimental saturation behaviour observed in our paper-based sensors. The saturating behaviour also indicates that above 5 nM chromium concentration, the amount of individual chromium ions in the paper saturates. In fact, the formation of Cr^{3+}–Cr^{3+} pairs at high chromium concentrations can be investigated, as it can shift the red emission towards the NIR region [55].

4. Conclusions

In summary, in this paper, we provide experimental evidence demonstrating how NIR to visible UCNPs can be used as luminescent nanosensors for the detection of low concentrations of Cr^{3+} in water. The ability to detect Cr^{3+} by the synthesised Yb, Er-NPs is based on the change in the red-to-green emission ratio due to Er^{3+} ions as the Cr^{3+} ion concentration in water increases. This ratiometric change is related to the different reabsorption of the red and green emission bands of Er^{3+} by the broad 580 nm visible absorption band of Cr^{3+} ions. As the NIR (980 nm) excitation (due to absorption of Yb^{3+} ions) avoids any auto-fluorescence related to a given substrate, a paper-based device was fabricated by incorporating non-functionalised Yb, Er NPs in paper substrates. This device allows the detection of low concentrations of Cr^{3+}, with a LoD of 2 nM, for Cr^{3+} concentrations of up to approximately 0.5 μM. At higher Cr^{3+} concentrations, a saturation regime was observed. These results can be explained by the appearance of a UV-increasing absorption edge that changes the red-to-green absorption ratio with the concentration of Cr ions in the paper substrate.

This first proof of concept demonstrates the possibility of detecting low concentrations of Cr3+ in aqueous media using a simple and fast detection method by analysing ratiometric luminescence changes of Yb, Er-NPs as the concentration of Cr3+ ions is increased.

CRediT authorship contribution statement

Gabriel López-Peña: Writing – review & editing, Writing – original draft, Methodology, Investigation. **Alejandro Rodríguez García:** Writing – review & editing, Investigation. **José García Solé:** Writing – review & editing, Writing – original draft. **Emma Martín Rodríguez:** Writing – review & editing, Writing – original draft, Validation, Supervision, Project administration, Funding acquisition, Conceptualization.

Declaration of competing interest

The authors declare that they have no known competing financial interests or personal relationships that could have appeared to influence the work reported in this paper.

Data availability
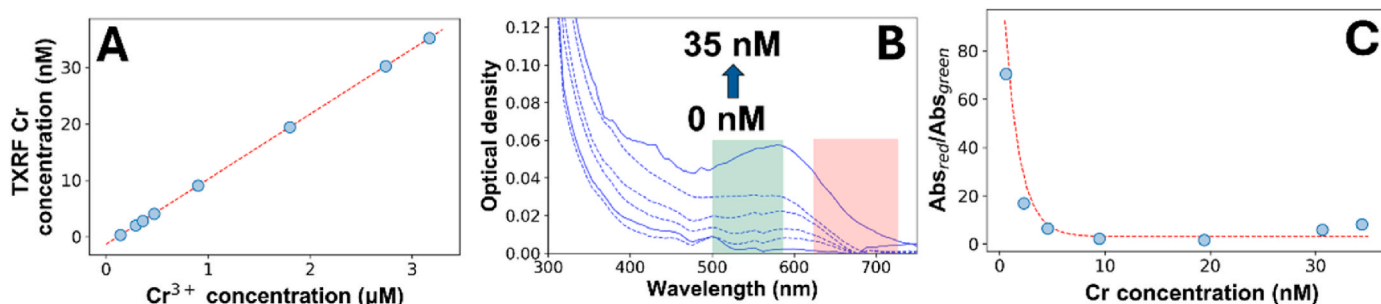
Data will be made available on request.

Fig. 4. A. *Cr^{3+} concentration in the paper substrate (measured by TXRF) as a function of Cr^{3+} concentration in aqueous solutions. The red dotted line was used as a guide for the eye.* **B.** *Absorption spectra of the paper substrate for different concentrations of chromium in the paper.* **C.** *Red-to-green absorption ratio areas (shadowed regions in B) as a function of Cr^{3+} concentration in the paper. The red dotted line was used as a guide for the eye.*

Appendix A. Supplementary data

Supplementary data to this article can be found online at https://doi.org/10.1016/j.jlumin.2024.120701.

References

[1] C.T. Kung, C.Y. Hou, Y.N. Wang, L.M. Fu, Microfluidic paper-based analytical devices for environmental analysis of soil, air, ecology and river water, Sens. Actuators, B 301 (2019), https://doi.org/10.1016/j.snb.2019.126855.

[2] Y. Lin, D. Gritsenko, S. Feng, Y.C. Teh, X. Lu, J. Xu, Detection of heavy metal by paper-based microfluidics, Biosens. Bioelectron. 83 (2016), https://doi.org/10.1016/j.bios.2016.04.061.

[3] J. Barnhart, Occurrences, uses, and properties of chromium, Regul. Toxicol. Pharmacol. 26 (1997), https://doi.org/10.1006/rtph.1997.1132.

[4] H.-H. Zeng, H. Wu, D. Peng, F. Liu, W.-G. Shi, J.-D. Qiu, Fast and selective detection of Cr(III) in environmental water samples using phosphovanadate Y(V0.2P0.8O4):Eu3+ fluorescence nanorods, ACS Sens. 3 (2018) 1569–1575, https://doi.org/10.1021/acssensors.8b00388.

[5] W. Chen, F. Cao, W. Zheng, Y. Tian, Y. Xianyu, P. Xu, W. Zhang, Z. Wang, K. Deng, X. Jiang, Detection of the nanomolar level of total Cr[(III) and (VI)] by functionalized gold nanoparticles and a smartphone with the assistance of theoretical calculation models, Nanoscale 7 (2015) 2042–2049, https://doi.org/10.1039/C4NR06726F.

[6] S.S.M. Hassan, M.N. Abbas, G.A.E. Moustafa, Hydrogen chromate PVC matrix membrane sensor for potentiometric determination of chromium(III) and chromium(VI) ions, Talanta 43 (1996) 797–804, https://doi.org/10.1016/0039-9140(95)01833-6.

[7] E.J. Arar, J.D. Pfaff, Determination of dissolved hexavalent chromium in industrial wastewater effluents by ion chromatography and post-column derivatization with diphenylcarbazide, J. Chromatogr. A 546 (1991) 335–340, https://doi.org/10.1016/S0021-9673(01)93031-6.

[8] N. Jie, Q. Zhang, J. Yang, X. Huang, Determination of chromium in waste-water and cast iron samples by fluorescence quenching of rhodamine 6G, Talanta 46 (1998) 215–219, https://doi.org/10.1016/S0039-9140(97)00261-0.

[9] F. Shemirani, M. Rajabi, Preconcentration of chromium(III) and speciation of chromium by electrothermal atomic absorption spectrometry using cellulose adsorbent, Fresenius' J. Anal. Chem. 371 (2001) 1037–1040, https://doi.org/10.1007/s002160101036.

[10] M. Sugiyama, O. Fujino, S. Kihara, M. Matsui, Preconcentration by dithiocarbamate extraction for determination of trace elements in natural waters by inductively-coupled plasma atomic emission spectrometry, Anal. Chim. Acta 181 (1986) 159–168, https://doi.org/10.1016/S0003-2670(00)85230-7.

[11] I. Turyan, D. Mandler, Selective determination of Cr(VI) by a self-assembled monolayer-based electrode, Anal. Chem. 69 (1997) 894–897, https://doi.org/10.1021/ac9607525.

[12] B. Demirata, I. Tor, H. Filik, H. Afşar, Separation of Cr(III) and Cr(VI) using melamine-formaldehyde resin and determination of both species in water by FAAS, Fresenius' J. Anal. Chem. 356 (1996) 375–377, https://doi.org/10.1007/s0021635603375.

[13] M.A. Zayed, B.N. Barsoum, A.E. Hassan, Spectrophotometric determination of iron and chromium in Cr-electroplating baths at the helwan engineering industrial company using pyrocatechol as indicator, Microchem. J. 54 (1996) 72–80, https://doi.org/10.1006/mchj.1996.0078.

[14] M. Shellaiah, T. Simon, K.W. Sun, F.-H. Ko, Simple bare gold nanoparticles for rapid colorimetric detection of Cr3+ ions in aqueous medium with real sample applications, Sensor. Actuator. B Chem. 226 (2016) 44–51, https://doi.org/10.1016/j.snb.2015.11.123.

[15] Karami, Changiz, Arkan, Elham, Sheikh ArabiMehdi, Desalination Water Treat., (n. d.). https://doi.org/10.5004/dwt.2019.24486.

[16] Z. Zhang, X. Ye, Q. Liu, Y. Liu, R. Liu, Colorimetric detection of Cr3+ based on gold nanoparticles functionalized with 4-mercaptobenzoic acid, J. Analytical Sci. Technol. 11 (2020) 10, https://doi.org/10.1186/s40543-020-00209-7.

[17] J.G. Solé, L.E. Bausá, D. Jaque, An Introduction to the Optical Spectroscopy of Inorganic Solids, 2005, https://doi.org/10.1002/0470016043.

[18] Y. Zhou, J. Zhang, L. Zhang, Q. Zhang, T. Ma, J. Niu, A rhodamine-based fluorescent enhancement chemosensor for the detection of Cr3+ in aqueous media, Dyes Pigments 97 (2013) 148–154, https://doi.org/10.1016/j.dyepig.2012.12.006.

[19] C. Huangfu, J. Hao, C. Hao, Highly Sensitive Fluorescent Probe for Cr3+ Detection Using Carbon Quantum Dots, Atlantis Press, 2018, pp. 871–877, https://doi.org/10.2991/ifeesm-17.2018.164.

[20] S. Borse, R. Rafique, Z.V.P. Murthy, T.J. Park, S.K. Kailasa, Applications of upconversion nanoparticles in analytical and biomedical sciences: a review, Analyst 147 (2022) 3155–3179, https://doi.org/10.1039/D1AN02170B.

[21] S. Hao, G. Chen, C. Yang, Sensing using rare-earth-doped upconversion nanoparticles, Theranostics 3 (2013) 331–345, https://doi.org/10.7150/thno.5305.

[22] B. Liu, H. Tan, Y. Chen, Upconversion nanoparticle-based fluorescence resonance energy transfer assay for Cr(III) ions in urine, Anal. Chim. Acta 761 (2013) 178–185, https://doi.org/10.1016/j.aca.2012.11.035.

[23] S. Liu, Y. Li, C. Zhang, L. Yang, T. Zhao, R. Zhang, C. Jiang, Upconversion color tuning in Ce3+-doped LiYF4:Yb3+/Ho3+@LiYF4 nanoparticles towards

[24] A.W. Martinez, S.T. Phillips, M.J. Butte, G.M. Whitesides, Patterned paper as a platform for inexpensive, low-volume, portable bioassays, Angew. Chem. Int. Ed. 46 (2007) 1318–1320, https://doi.org/10.1002/anie.200603817.

ratiometric fluorescence detection of chromium(III), J. Colloid Interface Sci. 493 (2017) 10–16, https://doi.org/10.1016/j.jcis.2017.01.022.

[25] W. He, M. You, W. Wan, F. Xu, F. Li, A. Li, Point-of-Care periodontitis testing: biomarkers, current technologies, and perspectives, Trends Biotechnol. 36 (2018), https://doi.org/10.1016/j.tibtech.2018.05.013.

[26] L.M. Fu, Y.N. Wang, Detection methods and applications of microfluidic paper-based analytical devices, TrAC, Trends Anal. Chem. 107 (2018), https://doi.org/10.1016/j.trac.2018.08.018.

[27] L. Feng, H. Li, L.-Y. Niu, Y.-S. Guan, C.-F. Duan, Y.-F. Guan, C.-H. Tung, Q.-Z. Yang, A fluorometric paper-based sensor array for the discrimination of heavy-metal ions, Talanta 108 (2013) 103–108, https://doi.org/10.1016/j.talanta.2013.02.073.

[28] R. Ding, Y.H. Cheong, A. Ahamed, G. Lisak, Heavy metals detection with paper-based electrochemical sensors, Anal. Chem. 93 (2021) 1880–1888, https://doi.org/10.1021/acs.analchem.0c04247.

[29] S.M.Z. Hossain, J.D. Brennan, β-Galactosidase-Based colorimetric paper sensor for determination of heavy metals, Anal. Chem. 83 (2011) 8772–8778, https://doi.org/10.1021/ac202290d.

[30] L. Zhang, L. Guan, Z. Lu, M. Li, J. Wu, R. Cao, J. Tian, Barrier-free patterned paper sensors for multiplexed heavy metal detection, Talanta 196 (2019) 408–414, https://doi.org/10.1016/j.talanta.2018.12.096.

[31] Q. Wang, Q. Yin, Y. Fan, L. Zhang, Y. Xu, O. Hu, X. Guo, Q. Shi, H. Fu, Y. She, Double quantum dots-nanoporphyrin fluorescence-visualized paper-based sensors for detecting organophosphorus pesticides, Talanta 199 (2019) 46–53, https://doi.org/10.1016/j.talanta.2019.02.023.

[32] F. Arduini, S. Cinti, V. Caratelli, L. Amendola, G. Palleschi, D. Moscone, Origami multiple paper-based electrochemical biosensors for pesticide detection, Biosens. Bioelectron. 126 (2019) 346–354, https://doi.org/10.1016/j.bios.2018.10.014.

[33] M.M. Bordbar, T.A. Nguyen, F. Arduini, H. Bagheri, A paper-based colorimetric sensor array for discrimination and simultaneous determination of organophosphate and carbamate pesticides in tap water, apple juice, and rice, Microchim. Acta 187 (2020) 621, https://doi.org/10.1007/s00604-020-04596-x.

[34] H. Chen, O. Hu, Y. Fan, L. Xu, L. Zhang, W. Lan, Y. Hu, X. Xie, L. Ma, Y. She, H. Fu, Fluorescence paper-based sensor for visual detection of carbamate pesticides in food based on CdTe quantum dot and nano ZnTPyP, Food Chem. 327 (2020) 127075, https://doi.org/10.1016/j.foodchem.2020.127075.

[35] M.O. Gorbunova, E.M. Bayan, A novel paper-based sensor for determination of halogens and halides by dynamic gas extraction, Talanta 199 (2019) 513–521, https://doi.org/10.1016/j.talanta.2019.02.093.

[36] M.O. Gorbunova, V.V. Apyari, A.A. Baulina, M.S. Garshina, M.S. Kulyaginova, A. V. Shevchenko, A.A. Furletov, S.G. Dmitrienko, Y.A. Zolotov, An improved step-by-step airflow/paper-based colorimetric method for highly selective determination of halides in complex matrices, Talanta 219 (2020), https://doi.org/10.1016/j.talanta.2020.121254.

[37] N. Bogdan, F. Vetrone, G.A. Ozin, J.A. Capobianco, Synthesis of ligand-free colloidally stable water dispersible brightly luminescent lanthanide-doped upconverting nanoparticles, Nano Lett. 11 (2011) 835–840, https://doi.org/10.1021/nl1041929.

[38] J.J. Janke, W.F.D. Bennett, D.P. Tieleman, Oleic acid phase behavior from molecular dynamics simulations, Langmuir 30 (2014) 10661–10667, https://doi.org/10.1021/la501962n.

[39] O.A.L. dos Santos, B. Pizzorno Backx, R.A. Abumousa, M. Bououdina, Environmental Implications Associated with the Development of Nanotechnology: from Synthesis to Disposal, Nanomaterials, 2022, https://doi.org/10.3390/nano12234319.

[40] T.M.D. Cao, T.T.G. Le, T.P.N. Nguyen, T.A.N. Dau, V.T. Nguyen, T.T.V. Tran, Investigating the effect of Yb3+ and Er3+ concentration on red/green luminescent ratio in β-NaYF4: Er, Yb nanocrystals using spectroscopic techniques, J. Mol. Struct. 1210 (2020) 128014, https://doi.org/10.1016/j.molstruc.2020.128014.

[41] D.T. Klier, M.U. Kumke, Analysing the effect of the crystal structure on upconversion luminescence in Yb3+,Er3+-co-doped NaYF4 nanomaterials, J. Mater. Chem. C 3 (2015) 11228–11238, https://doi.org/10.1039/C5TC02218E.

[42] M. Quintanilla, E. Hemmer, J. Marques-Hueso, S. Rohani, G. Lucchini, M. Wang, R. R. Zamani, V. Roddatis, A. Speghini, B.S. Richards, F. Vetrone, Cubic versus hexagonal – phase, size and morphology effects on the photoluminescence quantum yield of NaGdF 4 :Er 3+/Yb 3+ upconverting nanoparticles, Nanoscale 14 (2022) 1492–1504, https://doi.org/10.1039/D1NR06319G.

[43] L.U. Khan, Z.U. Khan, R.V. Rodrigues, L.S. da Costa, M. Gidlund, H.F. Brito, Synthesis and characterization of tunable color upconversion luminescence β-NaGdF4:Yb3+,Er3+ nanoparticles, J. Mater. Sci. Mater. Electron. 30 (2019) 16856–16863, https://doi.org/10.1007/s10854-019-01462-2.

[44] S. Balabhadra, M.F. Reid, V. Golovko, J.-P.R. Wells, A comparison of the Yb3+ absorption and upconversion excitation spectra for both the cubic and hexagonal phases of NaYF4:Yb3+/Er3+ nanoparticles, Opt. Mater. 107 (2020) 110050, https://doi.org/10.1016/j.optmat.2020.110050.

[45] Y.Z. Hamada, N. Makoni, H. Hamada, Three very different UV-VIS absorption spectra of three different transition metals found in biological solutions, Electron. J. Biol. S2 (2016) 6–9.

[46] N. Basavaraju, S. Sharma, A. Bessière, B. Viana, D. Gourier, K.R. Priolkar, Red persistent luminescence in MgGa 2 O 4 : Cr 3+ ; a new phosphor for **in vivo** imaging, J. Phys. Appl. Phys. 46 (2013) 375401, https://doi.org/10.1088/0022-3727/46/37/375401.

[47] Evan Sarina, Tanabe-Sugano Diagrams, 2020. https://chem.libretexts.org/Bookshelves/Inorganic_Chemistry/Supplemental_Modules_and_Websites_(Inorganic_Chemistry)/Crystal_Field_Theory/Tanabe-Sugano_Diagrams.

[48] Y.Z. Hamada, B.L. Carlson, J.T. Shank, Potentiometric and UV–vis spectroscopy studies of citrate with the hexaquo Fe3 + and Cr3 + metal ions, synthesis and reactivity in inorganic and metal-organic, Chemistry 33 (2003) 1425–1440, https://doi.org/10.1081/SIM-120024320.

[49] V. Roldán, J. Carlos González, M. Santoro, S. García, N. Casado, S. Olivera, J. C. Boggio, J.M. Salas-Peregrin, S. Signorella, L.F. Sala, Kinetics and mechanism of the oxidation of disaccharides by CrVI, Can. J. Chem. 80 (2002) 1676–1686, https://doi.org/10.1139/v02-187.

[50] D. Jaque, F. Vetrone, Luminescence nanothermometry, Nanoscale (2012), https://doi.org/10.1039/c2nr30764b.

[51] F. Vetrone, R. Naccache, A. Zamarrón, A. Juarranz de la Fuente, F. Sanz-Rodríguez, L. Martinez Maestro, E. Martín Rodriguez, D. Jaque, J. García Solé, J.

[52] Q. Mei, H. Jing, Y. Li, W. Yisibashaer, J. Chen, B. Nan Li, Y. Zhang, Smartphone based visual and quantitative assays on upconversional paper sensor, Biosens. Bioelectron. 75 (2016), https://doi.org/10.1016/j.bios.2015.08.054.

A. Capobianco, Temperature sensing using fluorescent nanothermometers, ACS Nano 4 (2010) 3254–3258, https://doi.org/10.1021/nn100244a.

[53] R. Arppe, I. Hyppänen, N. Perälä, R. Peltomaa, M. Kaiser, C. Würth, S. Christ, U. Resch-Genger, M. Schäferling, T. Soukka, Quenching of the upconversion luminescence of NaYF $_4$:Yb $^{3+}$,Er $^{3+}$ and NaYF $_4$:Yb $^{3+}$,Tm $^{3+}$ nanophosphors by water: the role of the sensitizer Yb $^{3+}$ in nonradiative relaxation, Nanoscale 7 (2015) 11746–11757, https://doi.org/10.1039/C5NR02100F.

[54] R. Fernández-Ruiz, TXRF spectrometry in the bioanalytical sciences: a brief review, X Ray Spectrom. 51 (2022), https://doi.org/10.1002/xrs.3243.

[55] S. Liu, J. Du, Z. Song, C. Ma, Q. Liu, Intervalence charge transfer of Cr3+-Cr3+ aggregation for NIR-II luminescence, Light Sci. Appl. 12 (2023) 181, https://doi.org/10.1038/s41377-023-01219-x.